Calculations of the free energy of dislocation defects in lamellae forming diblock copolymers using thermodynamic integration

Andrew J. Peters
Richard A. Lawson
Benjamin D. Nation
Peter J. Ludovice
Clifford L. Henderson

SPIE.

Calculations of the free energy of dislocation defects in lamellae forming diblock copolymers using thermodynamic integration

Andrew J. Peters, Richard A. Lawson, Benjamin D. Nation, Peter J. Ludovice, and Clifford L. Henderson*
Georgia Institute of Technology, School of Chemical and Biomolecular Engineering, 311 Ferst Drive NW, Atlanta, Georgia 30332-0100, United States

Abstract. State-of-the-art directed self-assembly (DSA) of block copolymer (BCP) methods still yield defect densities orders of magnitude higher than is necessary in semiconductor fabrication. The defect free energy of a dislocation pair or jog defect, one of the most common defects found in BCP-DSA, is calculated via thermodynamic integration using a coarse-grained molecular dynamics model as a function of χ and the degree of polymerization (N). It is found that χN is not the best predictor of defect free energy and that a single χN value can yield vastly different free energies when χ and N are different. Defect free energy was highly dependent on defect location relative to the underlayer, and free energy differences $\sim$100 kT were found among the three possible defect locations on a 1:3 guiding pattern. It was found that increasing molar mass dispersity (Đ) significantly reduced defect free energy. Extrapolating from Đ up to 1.5 suggests that the defect will occur in equal proportions to the defect free state at a Đ of around 1.6 for this system. It was found that long chains tended to concentrate near the defect and stabilize the defect. © *2016 Society of Photo-Optical Instrumentation Engineers (SPIE)* [DOI: 10.1117/1.JMM.15.2.023505]

Keywords: thermodynamic integration; directed self-assembly; defect; dislocation; coarse-grained.

Paper 15157P received Oct. 15, 2015; accepted for publication Apr. 5, 2016; published online May 10, 2016.

1 Introduction

Block copolymer (BCP) directed self-assembly (DSA) is a technique that has been studied extensively in recent years for use in nanofabrication because it excels in rapidly producing nanoscale patterns with long-range order when aligned to a prepatterned underlayer.[1,2] The most common methods to align such BCPs include using a chemically patterned underlayer,[3] a topographically patterned underlayer,[4] or some combination of the two.[5,6] Such techniques are being engineered to be more capable of producing useful patterns including aligned lamellae and cylinder phases that mimic the types of patterns useful in semiconductor device fabrication, but many obstacles still exist to their practical use industrially. One of the most critical obstacles is that of defect density. Progress has been made toward understanding the fundamental cause of these defects,[7–9] including the calculation of the defect free energy (ΔF) using a self-consistent field theory model in laterally confined systems[7] and how this free energy changes as a function of guiding linewidth.[7] In the context of such laterally confined systems, the effect of molar mass dispersity (Đ) was studied,[7] but only for binary blends, which is a poor model for the dispersity inherent in a typical BCP system. Work using a coarse-grained model has studied the effect of pattern-guiding strength on a 1:1 pattern.[8] However, current defect concentrations are orders of magnitude above necessary levels for many microelectronic applications[10,11] and the effects of numerous variables, including χ (the Flory Huggins interaction parameter), χN (where N is the degree of polymerization), and various guiding layer properties on defect formation are still not understood.

The study of these DSA problems can be aided greatly by the use of computer simulations, particularly in the area of defect modeling. Differentiating guiding pattern effects from inherent BCP defects and from particle or other contaminating factors is very difficult experimentally. Furthermore, the identification of the equilibrium defectivity and separating that from kinetic aspects of defect formation and annihilation is difficult, but crucial to understanding BCP defects and removing them in BCP-DSA processes. Simulations can much more easily achieve these goals. By using thermodynamic integration, coarse-grained molecular dynamics simulations can provide calculation of the free energy difference between two states, although a reversible path between them must be formulated. The free energy of a defect can be calculated as a function of various polymer and underlayer properties to provide insight into what property variations might minimize the occurrence of defects. This insight can then be applied to focus experimental investigations.

This work will study one of the most common defects found in BCP-DSA processes, a dislocation pair, or jog defect. This defect is shown in Fig. 1 and has been observed in various experiments[7–9,12,13] and in our own simulations. A dislocation pair (a dislocation is the "Y" structure in cyan in Fig. 1) can be separated by different numbers of lamellae, but this work will study a defect separated by a single domain, which is quite commonly seen in BCP-DSA.

While such defects occur for various pattern types and various polymers, a good understanding of how these patterns and polymer properties actually affect defect density is lacking. The defect density (n_d) can be described as

*Address all correspondence to: Clifford L. Henderson, E-mail: cliff.henderson@chbe.gatech.edu

Fig. 1 Top bottom image of the defect type studied in this paper. This is a common defect found in the literature.[7–9,12,13] The *A* beads are shown in white, while the *B* beads are shown in cyan.

$$n_{\mathrm{d}} \approx a_c^{-2} \exp\left(-\frac{\Delta F}{kT}\right), \tag{1}$$

where ΔF is the free energy between the defective state and the defect free state, k is the Boltzmann's constant, T is the absolute temperature, and a_c^2 is the area of the defect (about the repeat distance of the lamellae squared).[7–9,14,15] Because of the exponential dependence of defect levels on the defect free energy ΔF, accurate estimations of this parameter are critical to understanding anticipated defect levels in DSA processes.

2 Models and Methods

2.1 Coarse-Grained Model

A coarse-grained polymer model has been used and is described in detail elsewhere,[16,17] but a brief description will be given here. Molecules are coarse-grained by modeling four monomeric units as a single bead. Four monomers were chosen because this approximately corresponds to the statistical segment length of polystyrene and poly(methyl methacrylate), two common polymers studied in BCP DSA. Beads were connected using harmonic potentials. A harmonic angle potential was also used between every set of three consecutively bonded beads to prevent collapse due to nonbonded interactions. Every pair of beads that does not participate in the same angle potential (i.e., every bead that is on a different molecule or that is more than two bonds away) interact via a nonbonded potential similar to a Lennard–Jones potential as

$$E_{\mathrm{Nonbonded}} = \varepsilon_{ij}\left[\left(\frac{\sigma_{ij}}{r}\right)^8 - 2\left(\frac{\sigma_{ij}}{r}\right)^4\right]. \tag{2}$$

The parameter ε_{ij} is the depth of the potential well, which corresponds to the strength of the interaction and to cohesive energy density. σ_{ij} is the location of the minimum of the potential, which controls the average spacing between non-covalently bonded beads and the density of the system. The exponents in Eq. (2) are lower than in the Lennard–Jones potential expression because these fit the coarse grain potential well and reflect the averaging effect of the coarse-grained potential. In this work, the parameters for both *A* and *B* blocks are chosen to roughly reproduce the density and segment distribution of polystyrene. ε_{AA} and ε_{BB} are set to 0.5 kcal/mol, while σ_{AA}, σ_{BB}, and σ_{AB} are set to 1.26 nm. The equilibrium bond length used for both *A* and *B* polymers was 0.82 nm with a harmonic strength of

100 kcal/mol · nm². The equilibrium angle used for both *A* and *B* polymers was $2\pi/3$ radians (120 deg) with a harmonic strength of 5 kcal/mol · radian². Simulations were run at 500 K, a realistic thermal anneal temperature for DSA-BCP systems, with a time step of 0.05 ps. Further discussion of these parameters can be found elsewhere.[16,18,19] Because ε_{AB} describes the interaction between unlike blocks, this parameter is used to determine the value of the Flory–Huggins enthalpic interaction parameter χ. To determine χ, we fit the structure factor (a component of the x-ray diffraction profile) to Leibler's theory for BCP scattering similar to its extraction from the experimental results.[20,21] The $\varepsilon_{AB} - \chi$ relation is extrapolated from this fit in the mixed state to lower ε_{AB} values. This gives a relation for χ as a function of ε_{AB}, N, and volume fraction of the *A* block which is important in understanding our results relative to other calculations that primarily describe their potentials with the χ parameter. Details of this method can be found elsewhere.[22] Justification for the linear extrapolation follows: χ is defined by Flory[23]

$$\chi = z\Delta w/kT, \tag{3}$$

where z is the coordination number, Δw is the exchange energy, k is the Boltzmann constant, and T is the temperature of the system. The exchange energy, Δw, is defined as the energy penalty for replacing an $A - A$ or a $B - B$ interaction with an $A - B$ interaction

$$\Delta w = w_{AB} - \frac{1}{2}(w_{AA} + w_{BB}), \tag{4}$$

where w_{AB} is the interaction energy between an *A* bead and a *B* bead. Since the interaction energy in this model is defined by the nonbonded potential parameter ε, Δw can be defined for our system as

$$\Delta w = \varepsilon_{AB} - \frac{1}{2}(\varepsilon_{AA} + \varepsilon_{BB}). \tag{5}$$

This shows that Δw scales linearly with changes in ε_{AB}. As long as the density of the $A - B$ interface does not significantly perturb the system, z, the coordination number (the number of beads a single bead interacts with), will remain a constant. Since kT is a constant, χ will scale linearly with ε_{AB} until z is perturbed by density variations at the $A - B$ interface. All simulations were run using the HOOMD-Blue software package[24,25] and visualized in VMD.[26] The natural parallelizability of MD simulations and the GPU optimization of HOOMD allows simulations on a GPU enabled computer to run up to 200 times faster than a desktop computer (Intel Core 2 Duo ~2 GHz, 2GB RAM).

The natural repeat distance L_0 of each set of χ and N is measured using the structure factor, which provides similar information to that of a scattering experiment.[22,27] The values of L_0 used here are shown in Fig. 2.

2.2 Thermodynamic Integration

A method similar to that used by de Pablo and coworkers[8] and Müeller and coworkers[28] was used to determine free energy changes. The free energy difference between two states can be calculated as
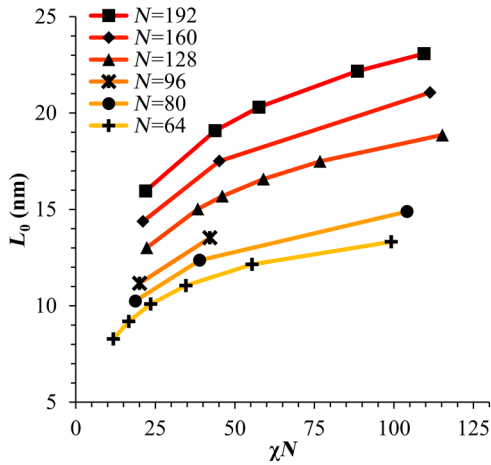
Fig. 2 Plot of L_0 dimensions as used in this work. Dimensions were measured using the structure factor.[22,27]

$$\Delta F_{a \to b} = \int_{u_A}^{u_B} \left\langle \frac{\delta H}{\delta u} \right\rangle \mathrm{d}u. \qquad (6)$$

H is the classical Hamiltonian of our model, u is any parameter that when varied defines a continuous, thermodynamically reversible path between state A and state B, and the brackets $\langle \cdot \rangle$; denote a thermodynamic average, that is the average value at equilibrium. The states used were a dislocation pair or jog defect (Fig. 1) and a defect free ordered lamellae state. Instead of trying to define a reversible, continuous path between a well-aligned lamellar state and a
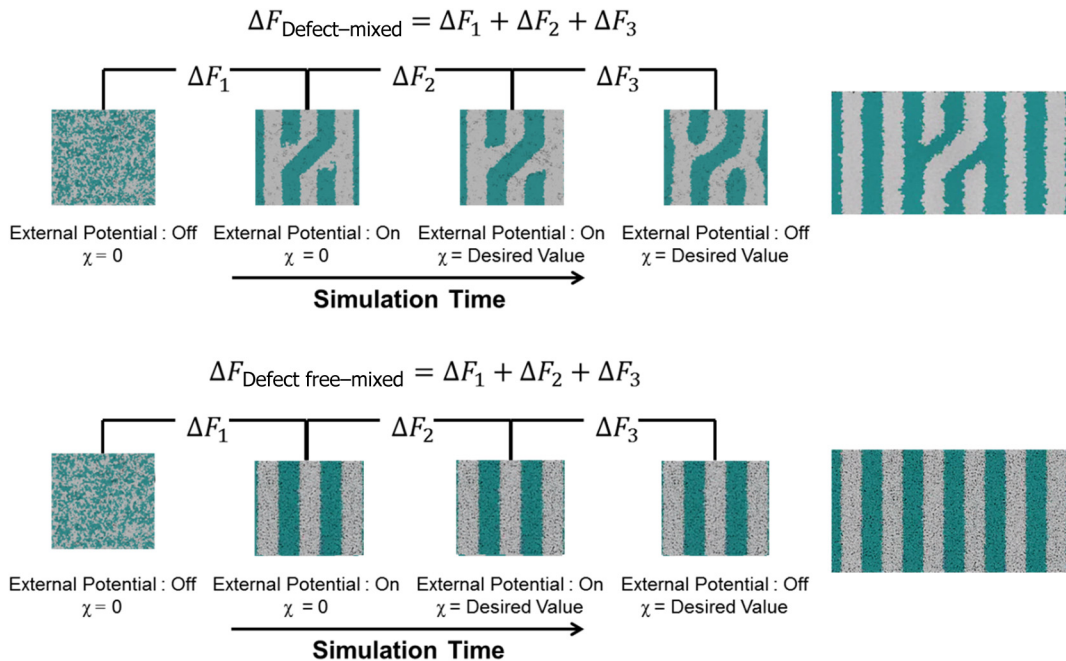
defect free state, it is easier for our model to use two different paths, i.e., a path from a mixed state to a lamellar state and a path from a mixed state to a defective state. Therefore in order to compare the defective and defect free states, two simulations were run as described in Fig. 3: one from a mixed state to a defect free lamellae state, which yields the free energy difference between the mixed state and the defect free state ($\Delta F_{\mathrm{DefectFree-Mixed}}$), and another simulation from a mixed state to a defective state, which yields the free energy difference between a mixed state and a defective state ($\Delta F_{\mathrm{Defect-Mixed}}$). Then

$$\Delta F_{\mathrm{Defect-DefectFree}} = \Delta F_{\mathrm{Defect-Mixed}} - \Delta F_{\mathrm{DefectFree-Mixed}}. \qquad (7)$$

Both $\Delta F_{\mathrm{Defect-Mixed}}$ and $\Delta F_{\mathrm{Defect-Free-Mixed}}$ were calculated using three branches of the MD simulation. The first branch is used to order the mixed polymers into the desired morphology. This was done using an external potential, which assigns an energy to beads based on their type and position within the simulation. In the case of the defect free state, the external potential energy was described as

$$U_{\mathrm{def-free}} = A \tanh \left[\frac{\cos\left(\frac{2\pi x}{L}\right)}{2\pi w} \right], \qquad (8)$$

where A is the strength of the potential, x is the position in the x axis of the bead, w is the width of the interface of the potential, and L is the repeat distance of the potential. The defect potential is created using the same equation, except the center portion is rotated 45 deg.

$$\Delta F_{\mathrm{Defect-mixed}} = \Delta F_1 + \Delta F_2 + \Delta F_3$$

$$\Delta F_{\mathrm{Defect\ free-mixed}} = \Delta F_1 + \Delta F_2 + \Delta F_3$$

Fig. 3 Schematic of the method used to calculate the defect free energy. Two simulations are run: one from the mixed to the defective lamellar state and one from the mixed to the defect free lamellar state. Each of these simulations yields the free energy difference between the mixed state and the corresponding final state. The difference between the two free energies is the free energy difference between the defect and the defect free state. Each simulation contains three branches over which a free energy difference is calculated. The first branch orders the system from the mixed state using an external potential, the second changes χ, and the third turns off the external potential.

$$U_{\text{def}} = \begin{cases} U_{\text{in}} & -0.75L_0 < x < 0.75L_0 \\ & -0.5L_0 < y < 0.5L_0 \\ U_{\text{out}} & \text{otherwise} \end{cases}, \tag{9}$$

$$U_{\text{in}} = A \tanh\left(\frac{\cos\left\{\frac{2\pi[x\cos(\pi/4)-y\sin(\pi/4)]}{L_0}\right\}}{2\pi w}\right), \tag{10}$$

$$U_{\text{out}} = A \tanh\left[\frac{\cos\left(\frac{2\pi x}{L_0}\right)}{2\pi w}\right]. \tag{11}$$

This produces the dislocation pair defect found in both our simulations and in published experimental results.[7–9,12,13] The integral from Eq. (6) was carried out where the reversible path (u) is defined by changes in the strength of the external potential, A. This integral, which yields ΔF_1 from Fig. 3, is shown in Eqs. (12) and (13) for the defect free case.

$$\Delta F_1 = \int_0^{A_{\text{max}}} \left\langle \frac{\delta U_{\text{def-free}}}{\delta A} \right\rangle dA = \int_0^{A_{\text{max}}} \left\langle \frac{U_{\text{def-free}}}{A} \right\rangle dA, \tag{12}$$

$$\Delta F_1 = \int_0^{A_{\text{max}}} \left\langle \tanh\left[\frac{\cos\left(\frac{2\pi x}{L_0}\right)}{2\pi w}\right] \right\rangle dA, \tag{13}$$

where A_{max} is 2.6. The defective case is identical except that $U_{\text{def-free}}$ is substituted for $U_{\text{def-free}}$.

The integrals [Eqs. (12) and (13)] were evaluated by numerically increasing A in 100 fixed-increment steps from 0 to A_{max}, which in this case was 2.6. At each step, an MD simulation is run at the new value of A until the simulation has equilibrated, and the average value at equilibrium is taken and used in integrating Eq. (13). In order to confirm the amount of time required to run the simulation at each step in the ramp up of A, multiple simulations were run for various lengths and the free energy integration was performed, as shown in Fig. 4. Short times showed significant deviations from the results at long times, because a short integration time does not allow the system sufficient time to equilibrate, making the path irreversible. At long times, the simulations are able to reach equilibrium at each step, and therefore the path is reversible and the measured free energy approaches a constant value. A value of 320,000 time steps per step in A was found to be sufficient and therefore was chosen to be used for the remainder of the paper. In Fig. 4 initially the value of the integrand is close to zero while the system is not well ordered. As the system phase separates due to the increasing strength of the external potential, the value of the integrand begins to approach a constant value. Figure 4 shows a sharp bend at $A \sim 0.4$. At this point, the system is mostly already phase separated, and the remainder of the simulation primarily consists of decreasing the interfacial roughness of the BCP.

Once the BCP has been ordered in the first branch of the simulation, χ (which was initially kept at zero during the first branch by setting $\varepsilon_{AB} = \varepsilon_{AA} = \varepsilon_{BB}$) must be increased. The starting condition had a χ of 0 so that the initial equilibrium
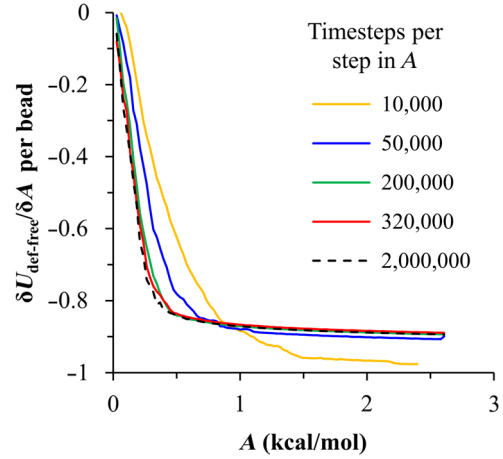
Fig. 4 Plot of the integrand of Eq. (13) as A is increased. As the number of timesteps per step in A is increased, the curves converge. A value of 320,000 was used to ensure accuracy and reasonable simulation times.

state of the system was a well-defined, well-mixed state. In our model, χ is controlled by changing only ε_{AB}, so ε_{AB} was varied from 0.5 kcal/mol ($\chi = 0$) to whatever value was desired, allowing the defect free energy to be calculated as a function of χ. Equation (6) was then integrated where u is now ε_{AB}, resulting in Eq. (14). This results in ΔF_2 from Fig. 3.

$$\Delta F_2 = \int_{0.5}^{\varepsilon_{AB\text{Final}}} \left\langle \frac{\delta U_{\text{nonbonded}}}{\delta \varepsilon_{AB}} \right\rangle d\varepsilon_{AB} = \int_{0.5}^{\varepsilon_{AB\text{Final}}} \left\langle \frac{U_{\text{nonbonded}}}{\varepsilon_{AB}} \right\rangle d\varepsilon_{AB}, \tag{14}$$

$$\Delta F_2 = \int_{0.5}^{\varepsilon_{AB\text{Final}}} \left[\left(\frac{\sigma_{AB}}{r}\right)^8 - 2\left(\frac{\sigma_{AB}}{r}\right)^4\right] \delta \varepsilon_{AB}. \tag{15}$$

$U_{\text{nonbonded}}$ is used because χ is changed via ε_{AB} and the nonbonded potential is the portion of the Hamiltonian in which ε_{AB} appears. The value $\varepsilon_{AB\text{Final}}$ is the value of ε_{AB} that yields the desired χ. This value will be less than the value of $\varepsilon_{AB} = 0.5$, which yields $\chi = 0$. The number of time steps per step in ε_{AB} was varied and the integrand measured as for branch 1. The results are found in Fig. 5. In this case, even very low numbers of timesteps per step in ε_{AB} yield the same result as very long runs. This is because there is little to no overall morphological change in this branch as there was in branch 1. This integration was done in 50 steps and run for 40,000 ps for each step in ε_{AB}.

The third and final branch of each simulation gradually turns off the external potential. Equation (6) was then integrated where u is A as A decreases from 2.6 to 0. This is described in Eq. (16).

$$\Delta F_3 = \int_{A_{\text{max}}}^0 \left\langle \tanh\left[\frac{\cos\left(\frac{2\pi x}{L}\right)}{2\pi w}\right] \right\rangle dA. \tag{16}$$

This is the same as Eq. (13) except that the integration limits have been switched. The same analysis as was done
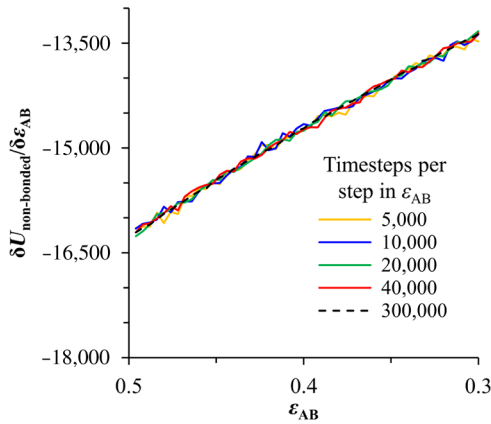
Fig. 5 Plot of the integrand of Eqs. (14) and (15) as ε_{AB} is increased. All values of time steps per step in ε_{AB} yield the same integrand.

in Fig. 4 is performed, the results of which are shown in Fig. 6. The integrand of Eq. (16) was calculated as a function of A as A was decreased for various numbers of time steps per step in A. Very low values of time steps per step in A show significant deviations, but values of 20,000 and greater all produce the same integrand. This is consistent with the smaller morphological changes in branches two and three relative to branch one. The first branch was changed from a mixed state to an ordered state, while the second branch underwent almost no morphological change as χ was increased. This third branch, where the external potential is removed but χ is kept high, undergoes some minor morphological changes because there are some slight differences between the form of the external potential and the true defect. Therefore this integration was done in 50 steps and run for 40,000 ps for each step in A.

The free energies of each of these branches for both the mixed to defect and mixed to defect free simulations were calculated. ΔF_1, ΔF_2, and ΔF_3 are summed together to yield $\Delta F_{\text{Defect−Mixed}}$ and $\Delta F_{\text{DefectFree−Mixed}}$ as in Eq. (7).
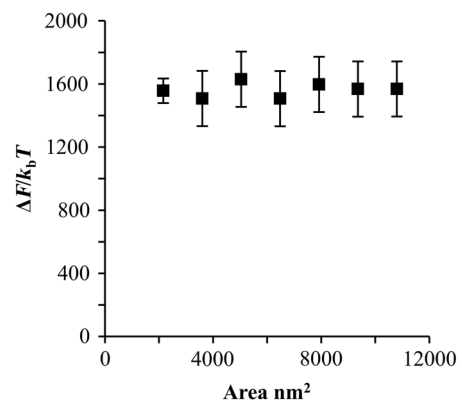
3 Results and Discussion

Various system sizes were simulated and the free energies were calculated to determine what system size was sufficient to accurately calculate the aforementioned free energy
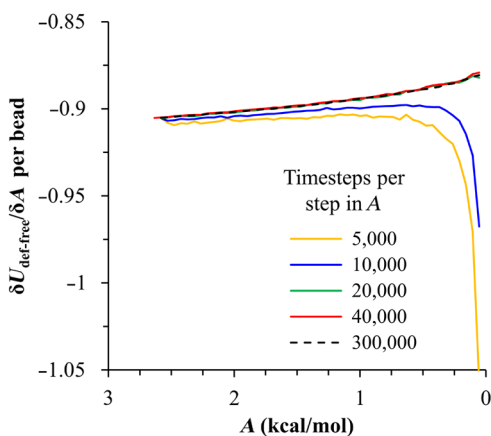
change. Box sizes in the x direction, the dimension perpendicular to the aligned lamellae, were restricted to multiples of L_0 to preserve periodicity and commensurability with the natural pitch of the BCP lamellae. Whenever this dimension dropped to $3L_0$ or less, then the defect became severely distorted and free energy could not be calculated. Similar distortions occurred when the y dimension decreased to very low values. Once the dimensions of the periodic box were greater than or equal to $5L_0$ in the x dimension and $3L_0$ in the y dimension, there did not seem to be a dependence of defect free energy on simulation area as shown in Fig. 7. This is very similar to box size constraints in the work of Nagpal et al.[8] In these free energy measurements, there is some run to run variation, which is shown using 90% confidence interval error bars. The variation is likely caused by incomplete sampling in the given timeframe of calculation. If a simulation is temporarily trapped in a transition state, then that state will likely be oversampled causing a deviation in the calculation for that run. On average, either over very long simulations or over many simulations, the sampling would average out to be correct, but in finite runs and simulation time, sampling will not be perfect.

In order to determine the effect of N and χ on the free energy of dislocation pairs, fully periodic simulations were run with box dimensions of $5L_0$ by $3L_0$ in the x and y dimensions and 15 nm in the film depth dimension. L_0 dimensions varied from ~8.3 to ~23.1 nm (because of variations in N and χ). N was varied from 64 monomers to 192 monomers at various χ values. The results are plotted as a function of χN in Fig. 8. Defect free energy is usually investigated and reported as a function of χN, as it is done by Takahashi et al.[7] However, as can be seen in this work (see Fig. 8), when both N and χ are varied the defect free energies do not fall onto a single curve as a function of χN, but in fact show great disparities in defect free energy at a single χN. Linear extrapolations of the data in Fig. 8 yield intercepts (where the free energy of the defect and defect free state are equal) of $\chi N \sim 2$ to ~11 for each N shown, but each set of N only has 2 to 5 data points so the fits are subject to some error. In addition, values of χN in this work generally stay above a χN of 20, in part because defects very near

Fig. 6 Plot of the integrand of Eq. (16) as A is decreased. Values of 20,000 timesteps per step in A and higher yielded the same integrand.

Fig. 7 Free energy of dislocation pair defect as a function of simulation size. Smaller simulation sizes resulted in deformed defects and made it impossible to calculate defect free energy. As long as the box size was at least $5L_0$ by $3L_0$ (area = 2160 nm²), the defect free energy did not vary significantly. The error bars shown are 90% confidence intervals over four or more simulations.
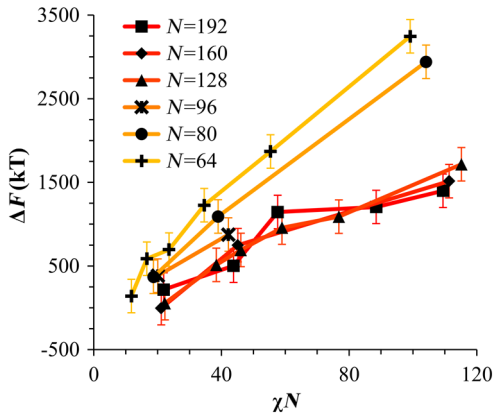
Fig. 8 The defect free energy as a function of χN. Overall, ΔF increases with χN, but there is a significant change with N. Defect free energy approaches 0 as χN approaches the ODT. Error bars represent 90% confidence interval.

the ODT had a tendency to very quickly heal themselves because of the very small or nonexistent barriers to defect healing.[22,29] However, the fact that the defect free energy approaches zero as the ODT is approached ($\chi N_{ODT} \sim 10.5$) makes sense because as the drive to phase separate becomes small, the energetic penalties associated with the defect will become less and less important.

The size of the defect, when the thickness is fixed, as it is here, scales with L_0^2, and so one might expect that the defect free energy would scale with χL_0^2. The size of the defect scales with L_0^2 while the penalty for the defect might scale with χ. However, as seen in Fig. 9(a), this scaling does not collapse the data to a single line. A second explanation for the variation might be that ΔF scales with the increase in interfacial energy due to an increase in interfacial area due to the presence of the defect. The increase in interfacial energy can be represented by $\chi \Delta I$, where ΔI is the difference in the $A - B$ interfacial area between the defective and defect free state. The interfacial area between A and B lines increases linearly with L_0 as

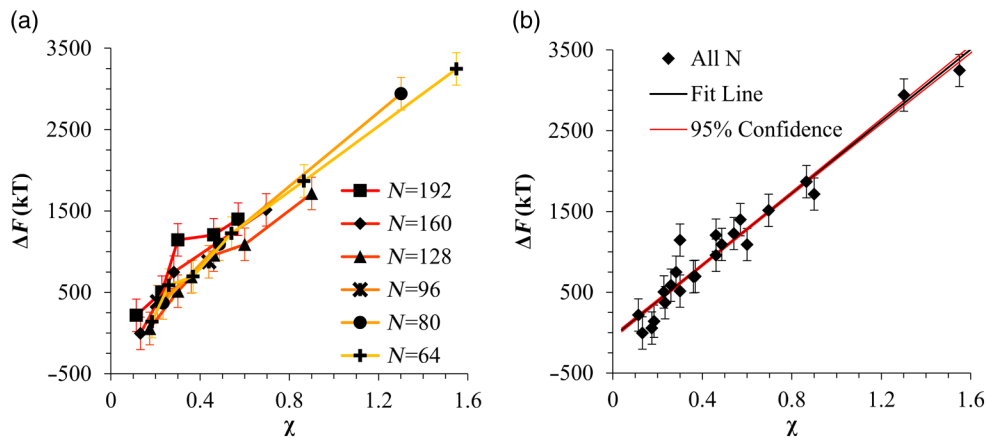$$\frac{\Delta I}{L_{thick}} = \frac{\pi}{2}L_0 + 2\sqrt{2}L_0 - 4L_0, \qquad (17)$$
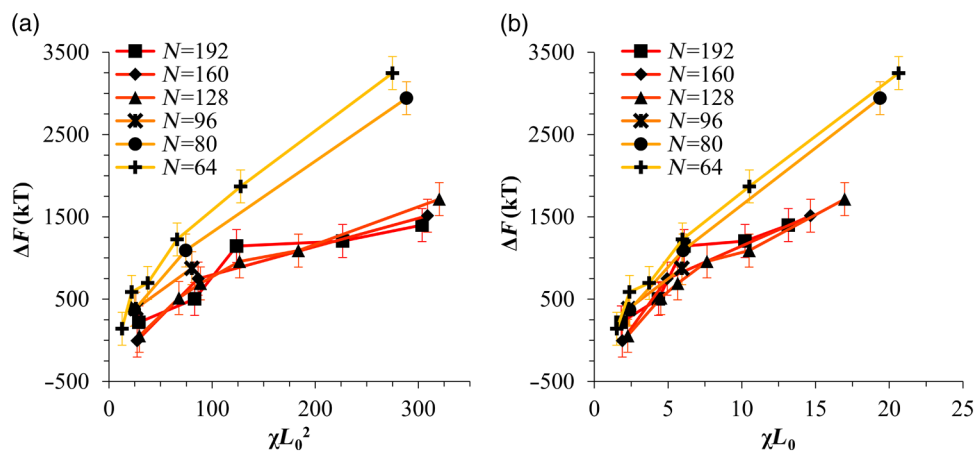
where L_{thick} is the thickness of the simulation. The first term refers to the interfacial area of the two terminated ends modeled as semicylinders. The second term refers to the interfacial area of the slanted lines in the middle of the defect, while the third term is the interfacial area of the defect free state within the hypothetical defect area. While this equation ignores some of the additional complexities of the dislocation pair defect, it is a good first-order approximation and shows that all terms scale with L_0. The penalty for this extra-interface will scale with χ, so a scaling of χL_0 would be expected if this were the only factor. However, as can be seen in Fig. 9(b), this scaling also fails to explain all of the variation between different χN values.

When the same data are plotted as a function of solely χ as in Fig. 10, the data appear to collapse to a single curve. This is very surprising as it seems L_0, and therefore N (which L_0 depends strongly) would be important as discussed above. There may be competing factors that appear to reduce the effect of N. For example, one might speculate that small chains may be stretched or compressed at the bends more than larger chains, which would increase the ΔF for low N, but the effect of L_0 (which scales with N^α where α is between 2/3 and ~ 1, depending on the value of χN[30]) increases ΔF for high N. These two factors would counteract each other, perhaps canceling each other out entirely. The idea that small chains are stretched or compressed more at the bends may be supported by the result that in polydisperse simulations, large chains concentrate near the bends and actually smooth the bends out some. This is shown later in this work in Fig. 14.

In order to produce smaller features, higher χ and lower N materials are required to reduce the associated pitch. At a similar χN value, but with a lower N and a larger χ, this data suggest the defect free energy will increase and therefore intrinsic defects will decrease. Previous work has shown that the energy barrier to defect removal is largely determined by χN regardless of N[22,29] and decreasing N will only speed up defect removal by increasing diffusive rates.[22] That is, keeping χN constant and reducing N will increase defect annihilation rate as well as decrease the number of stable defects that will form. This means that future generations of DSA will likely suffer from fewer defect problems, assuming similar quality underlayers can be made for

Fig. 9 Defect free energy plotted versus (a) χL_0^2 and (b) χL_0. Error bars are 90% confidence intervals.

(a)

(b)

Fig. 10 (a) The defect free energy as a function of χ. Defect free energy scales very well with χ with little dependence on N. Error bars show 90% confidence interval. (b) Fit line to the same data as in (a) with a 95% confidence interval on the fit shown as red lines.

smaller features. Comparing the calculations here to defect densities for a known BCP may be useful. Processes using polystyrene-b-poly(methyl methacrylate) (PS-b-PMMA), the most commonly studied BCP for DSA, have obtained defect densities on the order of 1 defect cm^{-2}.[10] Extrapolating a fit to the data in Fig. 10 to a χ value of 0.04 (approximately the χ for PS-b-PMMA[31]) and using Eq. (1), a defect density of $\sim$0.001 defects per cm^2 is obtained [using $(10 \text{ nm})^2$ for the defect size]. However, this calculation does not account for imperfection in the guiding layers, the BCP, or the processing environment, which could potentially increase the defect density by several orders of magnitude.[8] Accounting for these factors, and given the current state-of-the-art, experimentally achieved defect densities and the noise in this data, this calculated intrinsic defect density of PS-PMMA seems reasonable. Because the dependence of defect density on free energy is so strong, even a slight increase in χ and therefore in defect free energy results in defect densities that become vanishingly small.

The above results are obtained using fully periodic simulations so that the results are independent of guiding pattern. In order to explore the effect of guiding layers on defect free energy, thin film simulations were run. A thin film of BCP was placed over top of and in contact with a guiding layer composed of the same beads that compose the thin film of BCP. The underlayer was made to model a brush polymer covalently tethered to a hard substrate, as used previously.[17] An underlayer with 2× density multiplication, or a ratio of pinning stripe width to background region width of 1:3 was used. These underlayers are composed of a pinning stripe that is preferential to one block and is 0.5 L_0 wide and a background region that is 1.5 L_0 wide. The LiNe process uses a similar pattern.[3] Previous work by Nagpal et al.[8] studied the effect of underlayer interaction strength with the film in the context of at 1:1 pattern, that is alternating stripes each of width $L_0/2$. This type of pattern is not very useful in the context of semiconductor fabrication because the smallest feature size has already been achieved in the patterning of the underlayer (i.e., it does not multiple the density of the pattern). In industrially relevant processes at least one of the patterned stripes is wider than $L_0/2$ and the density of the pattern is multiplied via BCP-DSA. In processes, such as the LiNe process, the composition of the background region is varied to offer an

underlayer that is more neutral overall to prevent horizontal lamellae from forming.[19] Here, the effect of defect placement relative to the guiding pattern and the composition of the background region in the guiding pattern was measured, where the background region composition (C_b) refers to the percent of the background region composed of the same bead that compose the pinning stripe. So, if the pinning stripe is composed of A beads, then $C_b = 0\%$ means the background is all B beads, while C_b 50% means the background region is equally composed of A and B beads. The dislocation pair defect can occur at three places on such an underlayer as shown in Fig. 11. In the "A placement," the defect is centered on the pinning stripe. In the "B placement," the pinning stripe is on the edge of the defect. The pinning line is shown under the left side of the defect in Fig. 11, but because the defect is symmetric this is identical to putting the stripe under the right side of the defect. In the "C placement," the defect has the pinning stripes adjacent to both sides of the defect but not directly under the defect. Although the pinning stripes change from the B block, to the A block, and to the B block in Fig. 11, the A and B blocks are energetically identical so it is merely an expedient to keep the defect unchanged and centered in the simulation volume. Defect free energies were calculated on these underlayers through various background compositions and the results are shown in Fig. 12 for $N = 64$, $\chi N = 35$, and a film thickness of L_0 (11 nm for this specific N and χN).

The defect location relative to the pinning stripes makes a significant difference in the measured free energy. When the pinning stripe is under the center of the defect (A placement), the free energy penalty is highest, followed by the pinning stripe being under one side of the defect (B placement) and finally pinning stripes that surround the defect (C placement). This effect can be explained by looking at how many lines the pinning stripe is influencing. For the A case, the pinning stripe interacts directly with one line (the line above it) and indirectly with the two adjacent lines. On the other hand, while in the B case the defect still directly interacts with one line, it only indirectly interacts with one adjacent line, which decreases the influence of the pinning stripe on the defect free energy. Finally, the C case does not directly influence any lines participating in the defect, but indirectly influences two adjacent lines, which further lowers the free energy of the defect.

A Placement   B Placement   C Placement

Top-bottom of BCP Film

Top-bottom of Guiding Pattern
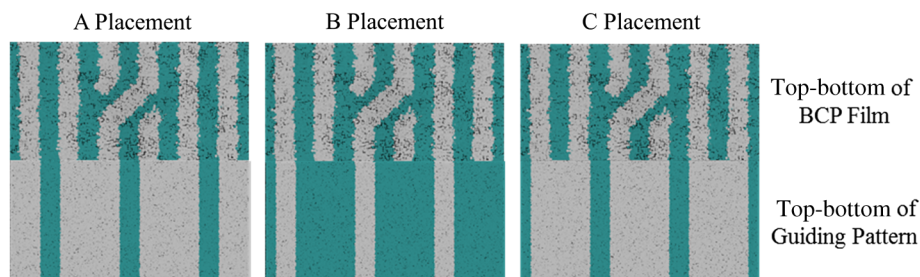
Fig. 11 Images of the three possible defect locations on a 1:3 guiding pattern.

The large differences in free energy as a function of defect placement relative to the underlayer (∼100 kT) on average means that the vast majority of defects will likely occur between pinning stripes (C placement) and not over top of them, although it appears that at higher background compositions defects with one edge over the pinning stripe (B placement) may appear in similar frequency. This result is significant because it is difficult to experimentally observe where defects form relative to the underlayer structure. At every background composition, the defects have very large penalties to form directly over the pinning stripe (A placement).

The effect of background region composition is not as clear. In the case of the A placement, background composition appears to have no significant effect on the free energy, while in the case of the B placement free energy appears to decrease with increasing C_b, and in the C placement free energy appears to increase with increasing C_b. However, the error bars are fairly large and make it difficult to claim such dependence with great certainty. From the simplest standpoint, where only the enthalpic interactions between the film and the underlayer are considered, the effect of C_b on the B placement makes sense. As C_b increases, the contrast (i.e., difference in composition) between the pinning stripe and the background region decreases and therefore decreases the guiding strength of the pattern. This would result in the defect free energy decreasing, as it is seen here. However, by this logic the defect free energy for the A placement should also decrease as C_b increases, but it does not. The C placement is different because no part of the defect directly touches the pinning
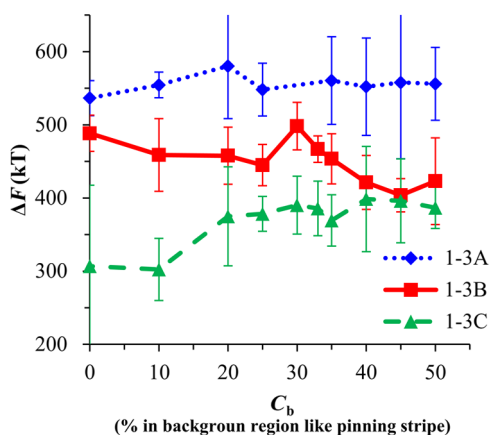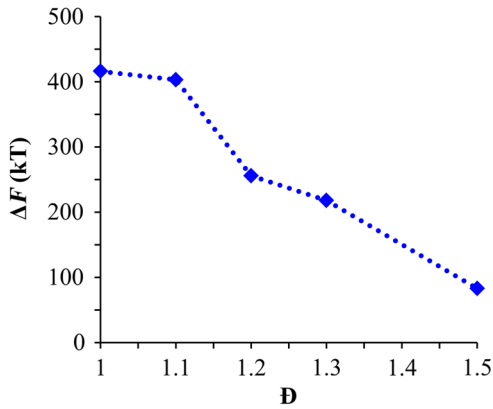
stripe in this simplified view, so the pinning stripe would not impose a driving force to fix the defect. Any effect it does have will be through some less obvious means. This all suggests that something more complicated than the simple enthalpic interactions of the film with the underlayer is required to understand the effect that C_b has on ΔF. In previous works, it has been found that the shape of the interfaces is strongly affected by the underlayer composition,[32] and changes at these interfaces have proven important in understanding the kinetics associated with defect removal.[31,32] In addition, these defects have a tendency to bend the lamellae slightly, even lamellae that are not immediately part of the defect (see Fig. 1: the first white lamellae not part of the defect are significantly bent) and the effect that this bend has on defect free energy is unclear. It may be that these interfacial changes are important to the defect free energy in these cases.

It should also be pointed out that these simulations have defect free energies less than half that of their periodic simulation counterparts (compare Fig. 12 with $N = 64$ and $\chi N = 35$ in Fig. 8). This is likely caused by the removal of interaction by the addition of the interfaces. Instead of having a dense polymer melt above and below the simulation volume, there is vacuum on one side and a thin brush on the other. This removes a large number of interactions that would affect the energy calculation. In addition, the density of the film near the free interface is depressed from its bulk density, further decreasing the overall number of interactions. Also, the fully periodic simulation is not analogous to a thin film on an unpatterned substrate because there are no interfaces, just interactions with the other side of the simulation volume. This means that the defect or defect free state essentially reinforces itself at the edge of the volume. The appearance of the film–underlayer interface and the film–vacuum interface plays an important role in defect free energy. This interface also proved critical in the study of defect healing kinetics.[10,31,33] We have also found that in some cases, defects that occur spontaneously have been accompanied by a local reduction in film thickness, but a thorough study has not yet been undertaken. This may also mean that film thickness plays an important role in defect free energy, but that was not directly studied here.
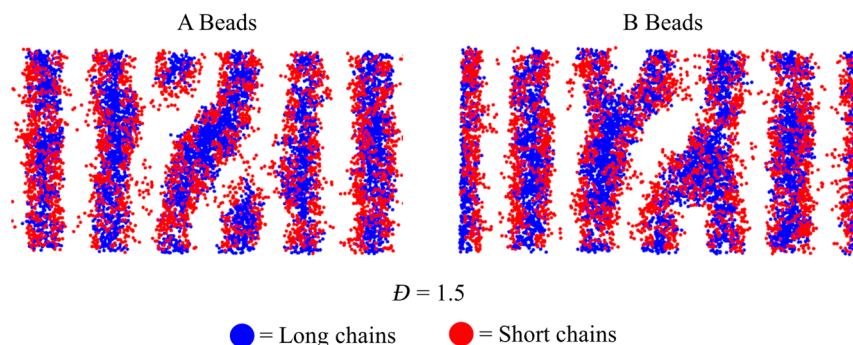
All simulations to this point were run with a molar mass dispersity (Đ) of 1, but in practice all BCPs have some molar mass dispersity. While it is expected that Đ can increase the defectivity of a BCP film, this effect has not been explored in much detail. Previous work by Takahashi et al.[7] studied the effect of Đ (using binary blends of polymers) on the defect free energy in laterally confined BCPs. They found a decrease in ΔF with Đ, and an interesting drop even at low Đ as the ratio of masses of the blended polymers

Fig. 12 Defect free energy as a function of background composition and defect location relative to the underlayer for $N = 64$, $\chi N = 35$, and a film thickness of L_0 (11 nm). Error bars refer to 90% confidence interval about the mean.

Fig. 13 Defect free energy as a function of Đ for $N = 64$ and $\chi N = 35$. The "B" defect location was used.

increased. However, using binary blends of polymers is very different from using a full distribution of lengths. Therefore, the effect that Đ had on defect free energy was investigated using these simulations. Simulations using the B placement at $X_N = 64$ (X_N is the number average degree of polymerization) and $\chi N = 35$ were built for various Đ using a Wesslau distribution with chains randomly dispersed through the simulation. Each chain was forced to have a volume fraction of 50% A and B. The resulting defect free energies are shown in Fig. 13. There is a significant reduction in free energy with increasing Đ, to the extent that the defect free energy may approach or cross zero in value if Đ were increased further. This implies that the defective state is as likely ($\Delta F = 0$) or more likely ($\Delta F < 0$) than the defect free state at very high Đ. At more commonly used Đ values (Đ = 1.1 or 1.2) the drop is still significant. At a Đ of 1.2, the defect free energy has dropped almost 40% and would correspond to orders of magnitude increase in defect density. The work by Takahashi et al.[7] saw a greater proportional drop at low Đ, but this drop in ΔF did not approach 0 at high dispersity. This is likely caused by the fact that they used binary blends. In that work, it was found that larger differences in chains lengths lead to larger drops in ΔF. For our model with a full distribution, larger dispersities will include chains lengths with larger differences in length between them and so the effects of both larger differences in chain lengths and a broader distribution of such chains are felt.

Figure 14 shows the locations of beads on long chains ($N > X_N$ where X_N is the average chain length) and short

chains ($N < X_N$) in a defect in a high dispersity case. There appears to be a higher concentration of long chains in the center of the defect than in the surrounding defect free areas. In addition, the defect seems more rounded and less angular than defects at lower dispersity. The distribution of various chain lengths appear to allow variations in line width (caused by variations in concentrations of chain lengths[34]) that allow for smoother lines. This may stabilize the defect in a way similar to the way homopolymer additions stabilize bends in patterned block polymers.[35] This would imply that homopolymer additions would increase defect density at equilibrium.

It should be pointed out that the external potential restricts almost all movement between lines so that chains are restricted to their original lines. They can move along an interface easily, but moving across an interface to another line would be a very rare event because of the high energetic penalty associated with moving a bead through the opposite typed domain. This has the effect of limiting variations in volume fraction and chain lengths from line to line through time. If at the actual lowest free energy state, the concentration of one length of chain is different near the defect as compared to far away from the defect, this distribution may not be properly sampled in the current simulations. This suggests the values calculated in Fig. 13 may be over estimates of the true defect free energy. A systematic examination of chain redistribution would discover if the lowest free energy state did redistribute some chains lengths closer to or farther from the defect. For example, creating a branch in the thermodynamic integration scheme that concentrated long or short chains near the defect, or increased the dispersity locally near the defect (but did not affect the overall dispersity) would help determine the distribution that would yield the lowest free energy state. However, such an examination was not performed here so the calculations show in Fig. 13 should be viewed as a maximum defect free energy.

4 Conclusions

The defect free energy of a dislocation pair or jog defect is calculated via thermodynamic integration using a coarse-grained molecular dynamics model as a function of χ and N. It was found that χN is not the best predictor of defect free energy and that a single χN value can yield vastly different free energies when χ and N are different (although their product is identical). This means that higher χ systems that are being produced to allow for smaller feature size DSA will likely have a lower equilibrium intrinsic defect density. Measurements of defect densities are reasonable for the

A Beads   B Beads

Đ = 1.5

● = Long chains   ● = Short chains

Fig. 14 Distribution of chain lengths for Đ = 1.5, $N = 64$, and $\chi N = 35$. Each point represents a single bead. The long chains tend to congregate near the defect.

oft-studied PS-PMMA. Defect free energies were measured as a function of defect placement relative to the underlayer and as a function of background composition. The effect of background composition was unclear but the defect free energy was highly dependent on defect location relative to the underlayer. Free energy differences of ~100 kT were found between the three possible defect locations on a 1:3 guiding pattern. The effect of Đ on defect free energy was also studied. It was found that Đ significantly reduced defect free energy. Long chains in a polydisperse sample tended to concentrate near and stabilize the defect.

References

1. M. P. Stoykovich and P. F. Nealey, "Block copolymers and conventional lithography," *Mater. Today* **9**(9), 20–29 (2006).
2. C. J. Hawker and T. P. Russell, "Block copolymer lithography: merging "bottom-up" with "top-down" processes," *MRS Bull.* **30**, 952–966 (2005).
3. C. C. Liu et al., "Integration of block copolymer directed assembly with 193 immersion lithography," *J. Vac. Sci. Technol. B* **28**, C6B30 (2010).
4. I. Bita et al., "Graphoepitaxy of self-assembled block copolymers on two-dimensional periodic patterned templates," *Science* **321**, 939–943 (2008).
5. J. Kim et al., "Toward high-performance quality meeting IC device manufacturing requirements with AZ SMART DSA process," *Proc. SPIE* **9423**, 94230R (2015).
6. Y. Kasahara et al., "RIE challenges for sub-15 nm line-and-space patterning using directed self-assembly lithography with coordinated line epitaxy (COOL) process," *Proc. SPIE* **9428**, 94280S (2015).
7. H. Takahashi et al., "Defectivity in laterally confined lamella-forming diblock copolymers: thermodynamic and kinetic aspects," *Macromolecules* **45**, 6253–6265 (2012).
8. U. Nagpal et al., "Free energy of defects in ordered assemblies of block copolymer domains," *ACS Macro Lett.* **1**, 418–422 (2012).
9. N. Laachi et al., "Self-consistent field theory of directed self-assembly in laterally confined lamellae-forming diblock copolymers," *Proc. SPIE* **8323**, 83230K (2012).
10. R. Gronheid et al., "Defect reduction and defect stability in IMEC's 14 nm half-pitch chemo-epitaxy DSA flow," *Proc. SPIE* **9049**, 904905 (2014).
11. R. Gronheid et al., "Implementation of templated DSA for via layer patterning at the 7nm node," *Proc. SPIE* **9423**, 942305 (2015).
12. C. Bencher et al., "Directed self-assembly defectivity assessment. Part II," *Proc. SPIE* **8323**, 83230N (2012).
13. D. B. Millward et al., "Graphoepitaxial and chemoepitaxial methods for creating line-space patterns at 33 nm pitch: comparison to a HVM process," *Proc. SPIE* **9423**, 942304 (2015).
14. J. Toner and D. R. Nelson, "Smectic, cholesteric, and Rayleigh-Benard order in two dimensions," *Phys. Rev. B* **23**, 316–334 (1981).
15. M. R. Hammond et al., "Temperature dependence of order, disorder, and defects in laterally confined diblock copolymer cylinder monolayers," *Macromolecules* **38**, 6575–6585 (2005).
16. R. A. Lawson et al., "Coarse grained molecular dynamics model of block copolymer directed self-assembly," *Proc. SPIE* **8680**, 86801Y (2013).
17. A. J. Peters et al., "Detailed molecular dynamics studies of block copolymer directed self-assembly: effect of guiding layer properties," *J. Vac. Sci. Technol. B* **31**, 06F302 (2013).
18. R. A. Lawson, P. J. Ludovice, and C. L. Henderson, "Development of realistic potentials for the simulation of directed self-assembly of PS-PMMA di-block copolymers," *Proc. SPIE* **7970**, 79700N (2011).
19. R. A. Lawson et al., "Simulation study of the effect of differences in block energy and density on the self-assembly of block copolymers," *J. Micro-Nanolith. Mem.* **13**, 031308 (2014).
20. S. Kim, P. F. Nealey, and F. S. Bates, "Decoupling bulk thermodynamics and wetting characteristics of block copolymer thin films," *ACS Macro Lett.* **1**, 11–14 (2012).
21. W. J. Durand et al., "Design of high-χ block copolymers for lithography," *J. Polym. Sci. Part A* **53**, 344–352 (2015).
22. A. J. Peters et al., "Coarse-grained molecular dynamics modeling of the kinetics of lamellar block copolymer defect annealing," *J. Micro/Nanolith. MEMS MOEMS* **15**, 013508 (2016).
23. P. Flory, *Principles of Polymer Chemistry*, Cornell University Press, Ithaca, New York (1953).
24. J. A. Anderson, C. D. Lorenz, and A. Travesset, "General purpose molecular dynamics simulations fully implemented on graphics processing units," *J. Comput. Phys.* **227**, 5342–5359 (2008).
25. "(HOOMD), Highly optimized object-oriented many-particle dynamics—Blue Edition," http://codeblue.umich.edu/hoomd-blue (February 2015).
26. W. Humphrey, A. Dalke, and K. Schulten, "VMD: visual molecular dynamics," *J. Mol. Graphics* **14**, 33–38 (1996).
27. F. S. Bates, J. H. Rosedale, and G. H. Fredrickson, "Fluctuation effects in a symmetric diblock copolymer near the order-disorder transition," *J. Chem. Phys.* **92**, 6255 (1990).
28. M. Müller and K. C. Daoulas, "Calculating the free energy of self-assembled structures by thermodynamic integration," *J. Chem. Phys.* **128**, 024903 (2008).
29. W. Li et al., "Defect removal in the course of directed self-assembly is facilitated in the vicinity of the order-disorder transition," *Phys. Rev. Lett.* **113**, 168301 (2014).
30. K. R. Shull, "Mean-field theory of block copolymers: bulk melts, surfaces, and thin films," *Macromolecules* **25**, 2122–2133 (1992).
31. Y. Zhao, E. Sivaniah, and T. Hashimoto, "SAXS analysis of the order–disorder transition and the interaction parameter of polystyrene-block-poly (methyl methacrylate)," *Macromolecules* **41**, 9948–9951 (2008).
32. B. D. Nation et al., "Effect of chemoepitaxial guiding underlayer design on the pattern quality and shape of aligned lamellae for fabrication of line-space patterns," *Proc. SPIE* **9423**, 94231J (2015).
33. R. Ruiz, R. L. Sandstrom, and C. T. Black, "Induced orientational order in symmetric diblock copolymer thin films," *Adv. Mater.* **19**, 587–591 (2007).
34. A. J. Peters et al., "Simulation study of the effect of molar mass dispersity on domain interfacial roughness in lamellae forming block copolymers for directed self-assembly," *Nanotechnology* **26**, 385301 (2015).
35. M. P. Stoykovich et al., "Directed assembly of block copolymer blends into nonregular device-oriented structures," *Science* **308**(5727), 1442–1446 (2005).

Andrew J. Peters recently completed his PhD on molecular dynamics simulations of block copolymer directed self-assembly with Professor Clifford L. Henderson at the Georgia Institute of Technology. He is now a postdoctoral associate under Timothy Lodge at the University of Minnesota. His research interests include both fundamental and applied aspects of self-assembling polymer systems, and he has studied BCP-DSA both experimentally and using molecular dynamics simulations.

Richard A. Lawson received his PhD in chemical engineering at Georgia Tech under the direction of Professor Clifford Henderson. He has worked in a number of areas related to patterning materials including design, synthesis, and characterization of photoresists, and block copolymers for directed self-assembly and has also done extensive work on resist and BCP simulation. After holding a postdoctoral position at Georgia Tech, he now holds a research position at Milliken and Company.

Benjamin D. Nation completed a BSc (Hons) in chemical engineering at Tennessee Tech University in 2012. He is currently undertaking a PhD on the simulation of block copolymer directed self-assembly with Professor Clifford L. Henderson at the Georgia Institute of Technology. His research interests include chemoepitaxial underlayer design, the effects of topography in BCP-DSA systems, and the effects of asymmetries in self-assembling BCP systems.

Peter J. Ludovice is an associate professor of chemical engineering at the Georgia Institute of Technology. After completing his BS and PhD degrees in chemical engineering from the University of Illinois, and M.I.T. respectively, he carried out molecular modeling research at the ETH-Zürich, IBM, NASA, and Molecular Simulations Inc., (now BIOVIA). His current research focuses on the computer simulation of synthetic and biological macromolecules.

Clifford L. Henderson is a professor in the School of Chemical and Biomolecular Engineering at the Georgia Institute of Technology and an adjunct professor in the School of Chemistry and Biochemistry at Georgia Tech. He received his BSc in chemical engineering with highest honors from the Georgia Institute of Technology and his MSc and PhD in chemical engineering from the University of Texas at Austin.